OPEN ACCESS
Journal of Innovative Optical Health Sciences
(2023) 2330004 (17 pages)
© The Author(s)
DOI: 10.1142/S1793545823300045

World Scientific
www.worldscientific.com

J. Innov. Opt. Health Sci. Downloaded from www.worldscientific.com
by UNIVERSITY OF ZARAGOZA on 08/22/23. Re-use and distribution is strictly not permitted, except for Open Access articles.

Depolarizing metrics in the biomedical field: Vision enhancement and classification of biological tissues

Mónica Canabal-Carbia*,‖, Albert Van Eeckhout†, Carla Rodríguez*, Emilio González-Arnay‡, Irene Estévez*, José J. Gil§, Enrique García-Caurel¶, Razvigor Ossikovski¶, Juan Campos* and Angel Lizana*

*Grup d'Òptica, Departamento de Fìsica
Universitat Autònoma de Barcelona, Bellaterra 08193, Spain

†ALBA Synchrotron Light Source
Carrer de la Llum 2-26, 08290
Cerdanyola del Vallès, Barcelona, Spain

‡Servicio deAnatomía Humana
Departamento de Ciencias Médicas Básicas
Universidad de La Laguna
Santa Cruz de Tenerife 38200, Spain

§Universidad de Zaragoza, Pedro Cerbuna 12
Zaragoza 50009, Spain

¶LPICM, CNRS, Ecole Polytechnique
Institut Politechnique de Paris, Palaiseau 91120, France
‖monica.canabal@uab.cat

Received 31 October 2022
Revised 13 December 2022
Accepted 15 January 2023
Published 23 February 2023

Polarimetry encompasses a collection of optical techniques broadly used in a variety of fields. Nowadays, such techniques have provided their suitability in the biomedical field through the study of the polarimetric response of biological samples (retardance, dichroism and depolarization) by measuring certain polarimetric observables. One of these features, depolarization, is mainly produced by scattering on samples, which is a predominant effect in turbid media as biological tissues. In turn, retardance and dichroic effects are produced by tissue anisotropies and can lead to depolarization too. Since depolarization is a predominant effect in tissue samples, we focus on studying different depolarization metrics for biomedical applications. We report the suitability of a set of depolarizing observables, the indices of polarimetric purity (IPPs), for biological tissue inspection. We review some results where we demonstrate that IPPs lead to

‖Corresponding author.

This is an Open Access article. It is distributed under the terms of the Creative Commons Attribution 4.0 (CC-BY) License. Further distribution of this work is permitted, provided the original work is properly cited.

better performance than the depolarization index, which is a well-established and commonly used depolarization observable in the literature. We also provide how IPPs are able to significantly enhance contrast between different tissue structures and even to reveal structures hidden by using standard intensity images. Finally, we also explore the classificatory potential of IPPs and other depolarizing observables for the discrimination of different tissues obtained from *ex vivo* chicken samples (muscle, tendon, myotendinous junction and bone), reaching accurate models for tissue classification.

Keywords: Polarimetry; indices of polarimetric purity; organic tissues visualization; artificial intelligence.

J. Innov. Opt. Health Sci. Downloaded from www.worldscientific.com
by UNIVERSITY OF ZARAGOZA on 08/22/23. Re-use and distribution is strictly not permitted, except for Open Access articles.

1. Introduction

Polarization is an intrinsic characteristic of transversal waves as it is the case of light; it can be used to study light-matter interactions and extract the response of samples to different states of polarization through polarimetric techniques. In the literature, we can find a great number of polarimetry applications in a wide variety of research fields, such pollution control, remote sensing, astronomy, or botanical applications.[1–5] Since polarimetric inspection of samples is a fast, noninvasive and nondestructive approach, these techniques are nowadays very useful in the field of biomedicine. In fact, some works have reported that the benefit of polarimetric tools for biomedical applications lies in the interaction of polarized light with different biological structures and their different polarimetric responses. In this way, biological tissues can be defined as a turbid medium formed by inhomogeneous complex structures leading to different physical properties related to polarization: retardance, dichroism and depolarization. This last phenomenon, depolarization, is a very predominant effect in biological tissues and it is caused by scattering processes in light-matter interactions. Multiple scattering is produced by the high concentration of scattering centers in biological tissues, that can be isotropic with different sizes and densities or to present intrinsic polarimetric characteristics as retardance, dichroism, etc. The specific characteristics of tissues that give rise to scattering processes are further described in the literature.[6] In turn, the anisotropic nature in the organization of some fibers composing the tissues, such as collagen and elastin among others, give biological tissues birefringent properties resulting in retardance.[7] Also, dichroism is present in biological molecules but its effects are less prominent than depolarization and retardance, as before mentioned.

Because of this suitability of polarimetric techniques for the study of biological tissues, they are nowadays widely used in biomedical applications. In this sense, some diseases, such as cancer, produce structural changes in the pathological tissues, and the polarimetric methods are capable of detecting such changes in a variety of pathologies.[8] For example, polarimetric observables have been used for the study of human cervix to differentiate normal and precancerous samples or to discriminate between nonpregnant and pregnant samples through the measurement of the collagen orientation for detecting at-risk pregnancies.[9,10] They are also useful for the study of tumor–stroma ratio for cancer in different tissues: breast, prostate or myocardium.[11–13] In addition, we can find several studies in skin tissues to differentiate normal and pathological skin.[14,15] Interestingly, some authors are taking advantage of polarimetric methods for *in vivo* patients in preoperatory stages or even during surgery. For instance, in the identification of white matter fiber tracks for delineating tumor borders during neurosurgery or the detection of skin cancer margins.[16,17] More information related to healthy and pathological tissue discrimination through polarimetric means can be found in Ref. 18. In addition, if readers are interested in a broad vision of the applications of polarization in biomedicine, they can address to some recent reviews in the field.[19–22] What is more, the usefulness of polarimetric methods to enhance the visualization of biological structures and pathologies is nowadays also used for the implementation of classification models in biomedical applications. In this sense, diverse authors have reported the interest of training classification algorithms with polarimetric observables, which lead to accurate classification models of tissues and pathologies.[23,24]

Importantly, in the framework of biomedical applications, the most used polarimetric observables

J. Innov. Opt. Health Sci. Downloaded from www.worldscientific.com
by UNIVERSITY OF ZARAGOZA on 08/22/23. Re-use and distribution is strictly not permitted, except for Open Access articles.

are devised to study sample anisotropies as retardance and/or dichroic (diattenuation and polarizance) properties of samples. In this sense, some authors even try to avoid the depolarization response of biological tissue, because they consider that depolarization masks the retardance and dichroic features of samples, being of interest for their applications.[6] However, in recent years, depolarization metrics have awakened a high interest in biomedical applications, as they provide fundamental and useful information about tissues themselves. In this vein, there are in literature several studies showing promising results and highlighting the potential of depolarizing channels for the visualization and classification of biological tissues.[24–27] Nowadays, the most widespread depolarizing metric used for biomedical applications is the degree of polarization (DoP).[28] Recently, a generalization of the DoP metric, the so-called depolarization index (P_Δ) is being used in multiple scenarios as it provides better results than DoP in terms of visualization.[29–31] This P_Δ has information on the overall depolarization response of samples.[32]

Nevertheless, in the literature, we can find different polarimetric parameters representing the depolarizing properties of a sample.[32,33] Some of them are able to provide larger image contrast and physical interpretation than P_Δ. In this paper, we review recent results of different works we conducted in the framework of biomedical applications of depolarization metrics. We demonstrate the high suitability of these metrics for vision enhancement of different biological tissues, as well as to implement classification models leading to accurate classification of tissues.[24,27,34–36] These methods can be of interest for different biomedical applications such as vision-guided surgery, tissue classification or pathology detection.

The outline of this paper is as follows. Section 2 introduces the mathematical description of the depolarization metrics used in this paper. In Sec. 3, we describe the experimental methods and materials employed in the revised works. In Sec. 4, we demonstrate the advantages of the indices of polarimetric purity (IPPs) in comparison with P_Δ, in terms of depolarizers discrimination. As biological tissues are particular cases of depolarizers, we also motivate the use of IPPs for image contrast enhancement of biological structures. In Sec. 5, we take advantage of the IPPs ability for image enhancing and discriminatory potential to build different pseudo-coloration models for biological structures' enhanced vision. Afterward, in Sec. 6, we propose different classification models based on classifiers and regression algorithms that are able to provide accurate classification of different tissue samples. The main conclusions of the work are provided in Sec. 7.

2. Mathematical Background

As stated in the introduction, depolarizing observables are valuable for a wide range of applications. In this section, we will describe different depolarization metrics and spaces inspecting the depolarizing properties of samples, and which are the basis of the papers reviewed in this work. Even though that one commonly used depolarization metric in biomedical applications is the depolarizing index P_Δ, we will describe five different sets of depolarizing parameters that have recently shown their usefulness for enhanced vision and classification. These parameters can be divided into two categories: (1) three sets of metrics based on the eigenvalues of the covariance matrix (H) (the IPPs, the natural space and the higher order parameters) and, (2) two sets of metrics based on the canonical depolarizers (the type I canonical parameters and the high-order Lorentz parameters).[32] From all those metrics, most results presented in this work are based on the IPPs, as they have shown to be especially suitable for vision enhancement in biomedical applications.

In the following subsections, some representative depolarizing observables are described. In particular, whereas those observables based on the eigenvalues of H are described in Sec. 2.1, those based on the canonical depolarizer are described in Sec. 2.2. In addition, in Sec. 2.3, we briefly describe the three-dimensional (3D) depolarization spaces, these being groups of three depolarizing metrics that can be associated to the cardinal axes, enclosing spaces where depolarizers can be represented.

2.1. *Depolarization observables based on the covariance matrix (H)*

The covariance matrix H is a Hermitian semi-define matrix that arises from a transformation of the Mueller matrix (M) and is defined as follows[32,37,38]:

$$H(M) = \frac{1}{4}\sum_{i,j=0}^{3} m_{ij}(\sigma_i \otimes \sigma_j^*), \tag{1}$$

J. Innov. Opt. Health Sci. Downloaded from www.worldscientific.com by UNIVERSITY OF ZARAGOZA on 08/22/23. Re-use and distribution is strictly not permitted, except for Open Access articles.

where m_{ij} represent the Mueller matrix elements, σ are the Pauli matrices and $\otimes$ is the Kronecker product. This transformation of M to H is convenient since H is a Hermitian matrix, and thus, diagonalizable, whereas the Mueller matrix is not necessarily diagonalizable. Both the IPPs and the parameters comprising the natural space are based on the eigenvalues of H. In the first case, the IPPs arise from lineal combinations of those eigenvalues and, the values conforming the natural space consist of three of the four eigenvalues of H. Interestingly, the eigenvalues of H are connected with the enpolarizing and depolarizing properties of samples.[32]

The four eigenvalues of $H(\lambda_i)$ provide the basis for a decomposition of the Mueller matrix, the so-called Cloude parallel decomposition[32,37]:

$$M = \sum_{i=1}^{4} \lambda_i M_i, \tag{2}$$

where M_i are pure matrices and, the coefficients λ_i are the eigenvalues of H. To fulfill the condition of a physically realizable M, the eigenvalues must satisfy Cloude's criterion[38]:

$$0 \leq \lambda_4 \leq \lambda_3 \leq \lambda_2 \leq \lambda_1, \tag{3}$$

$$\sum_{i=1}^{4} \lambda_i = 1. \tag{4}$$

The combination of Eqs. (3) and (4) allows us to eliminate one eigenvalue resulting in:

$$0 \leq \lambda_4 \leq \lambda_3 \leq \lambda_2 \leq 1 - \lambda_4 - \lambda_3 - \lambda_2. \tag{5}$$

With this constraint, we achieve the three parameters defining the natural space $(\lambda_4, \lambda_3, \lambda_2)$.

The second set of metrics that we can define from these eigenvalues are the IPPs, labeled as P_n, $n = 1, 2, 3$ and defined by[39]:

$$P_n = \sum_{k=1}^{n} k \Delta\lambda_k, \tag{6}$$

where $\Delta\lambda_k = \lambda_k - \lambda_{k+1}$. The constraints from Eq. (5) lead to the following condition on the IPPs:

$$0 \leq P_1 \leq P_2 \leq P_3 \leq 1. \tag{7}$$

Another well-known depolarizing observable reported in the literature is the so-called depolarizing index P_Δ, which results in a generalization of the DoP to matrices.[32] The P_Δ is an overall measure of the depolarizing properties of a sample. It is restricted from 0 to 1, being the value 1 associated to fully polarized samples and the value 0 to fully depolarized ones. This metric can be written in terms of the IPPs as follows[40]:

$$P_\Delta = \frac{1}{\sqrt{3}} \sqrt{2P_1^2 + \frac{2}{3}P_2^2 + \frac{1}{3}P_3^2}. \tag{8}$$

In turn, the parallel decomposition in Eq. (2) can be rewritten as a function of the IPPs in the following way[32,41]:

$$M = P_1 M_{J0} + (P_1 - P_2)M_1 + (P_3 - P_2)M_2 + (1 - P_2)M_3, \tag{9}$$

where P_1 acts as the weight of the nondepolarizing component M_{J0}, $P_2 - P_1$ and $P_3 - P_2$ are the portions of the medium behaving as a two-dimensional (2D) depolarizer and a 3D depolarizer, respectively, and $1 - P_3$ is the portion of the medium acting as a pure depolarizer. In this way, we can state how the IPPs (and consequently, the eigenvalues of H) are directly related to different sources of depolarization. Therefore, in comparison with the parameter P_Δ, the IPPs not only further synthesize the information (we go from one information channel to three) but also provide a larger physical interpretation of depolarizing processes.

The last observables reviewed in this subsection are the depolarization indices of higher order, which are a generalization of the depolarizing index P_Δ.[33] Whereas the IPPs are defined from a linear combination of H eigenvalues, the high-order depolarization indices $(P_\Delta, P_\Delta^{(3)}, P_\Delta^{(4)})$ are a nonlinear combination of them:

$$P_\Delta^{(m)} = \sqrt{\frac{1}{4^{m-1} - 1}\left(4^{m-1} \sum_{k=1}^{4} \lambda_k^m - 1\right)}, \tag{10}$$

where

$$0 \leq \cdots \leq P_\Delta^{(m)} \leq \cdots \leq P_\Delta^{(3)} \leq P_\Delta \leq 1. \tag{11}$$

Note that when $m = 2$, we retrieve Eq. (8), this being therefore a particular case of Eq. (10).

2.2. *Depolarization observables based on type I canonical depolarizer parameters*

This second group of depolarization metrics and associated metric triplets (depolarization spaces)

J. Innov. Opt. Health Sci. Downloaded from www.worldscientific.com by UNIVERSITY OF ZARAGOZA on 08/22/23. Re-use and distribution is strictly not permitted, except for Open Access articles.

are based on model matrices called canonical depolarizers.[42]

The first set of canonical depolarizing metrics we revise is the so-called type I canonical depolarizers. To determine these metrics Mueller matrices are first decomposed into different constituent parts, and the associated depolarizer Mueller matrix, $M_{\Delta d}$, is calculated.[43] Afterward, the covariance matrix $H_{\Delta d}$ associated to $M_{\Delta d}$ is calculated according to Eq. (1). The metrics of the canonical space (d_1, d_2, d_3) are constructed by linear combinations of the $H_{\Delta d}$ eigenvalues λ_i'[33]:

$$d_1 = 1 - 2\lambda_3' - 2\lambda_4', \tag{12}$$

$$d_2 = 1 - 2\lambda_2' - 2\lambda_4', \tag{13}$$

$$d_3 = 1 - 2\lambda_2' - 2\lambda_3', \tag{14}$$

whose values are restricted to $|d_3| \leq d_2 \leq d_1 \leq 1$ due to Eq. (3). Finally, we describe another reported set of metrics derived from the canonical depolarizer. In particular, the so-called type I Lorentz space is composed of three parameters $(L_I, L_I^{(3)}, L_I^{(4)})$ which are defined by nonlinear combinations of the type I canonical depolarizer parameters[33]:

$$L_1^{(m)} = \sqrt{\frac{1}{4^{m-1}-1}\left[4^{m-1}\frac{1 + d_1^{2m} + d_2^{2m} + d_3^{2m}}{(1 + d_1^2 + d_2^2 + d_3^2)} - 1\right]}. \tag{15}$$

2.3. *Depolarization spaces*

In Secs. 2.1 and 2.2, we have reported different triplets of depolarizing observables with the metrics' values ranging from 0 to 1, and with their respective restrictions due to the relations between variables. Under this scenario, different 3D depolarization spaces can be defined from each of these depolarizing triplets, associating each metric of the triplet to an axis in the 3D Cartesian space. The resulting spaces, considering the specific restrictions for each studied observables triplet, lead to particular volumes within the Cartesian space, where the different depolarizers can be represented. In all the cases, the three triplets reviewed in Sec. 2.1 (the natural, the IPPs and the high-order depolarization indices spaces) and two triplets reviewed in Sec. 2.2 (Type I Canonical depolarizers and Type I Lorentz spaces) lead to five different tetrahedrons whose specific volume is constrained by the particular relations between the variables in each case.[27] The volumes inside the tetrahedrons contain all the possible physically realizable depolarizers, each one of them catalogued by a particular triplet of values for the corresponding depolarizing space. Interestingly, the spaces corresponding to the H eigenvalues, the natural space, the IPPs and the type I canonical metrics, are linear spaces, whereas the high-order depolarization indices and the type I Lorentz spaces are nonlinear.[27,33] In the linear spaces, the relation between the variables conforming the limits of the tetrahedron is linear, therefore, the limiting surfaces are plane, whereas in the nonlinear case the relation between the variables is nonlinear and the bounding surfaces conforming the volume are nonlinear. As shown in Ref. 27, the linear spaces enclose larger volumes inside the tetrahedrons than nonlinear spaces, being the Purity Space, associated to the IPPs, the one presenting a larger volume. Note that larger volumes tend to increase distances between two different depolarizers (representing, for instance, different tissue responses) and this situation may be associated to better performance in terms of discriminatory potential. For this reason, many times the IPPs are preferred to be used for the visualization of biological tissues, this being also the case in some of the studies and results shown in the following sections.

3. Materials and Methods

In this section, we present the description of the experimental setup used to measure the Mueller matrices of the inspected samples (Sec. 3.1). Moreover, in Sec. 3.2, we explain the sample preparation process pre and post measure.

3.1. *Experimental setup description: Complete image Mueller matrix polarimeter*

In this section, we will describe the experimental setup used to obtain the experimental Mueller matrices of the samples analyzed in this work.

The experimental Mueller matrices of the samples analyzed in this text are obtained by means of a complete image Mueller matrix polarimeter. The polarimeter is comprised of two separated mobile arms which are named the polarization state generator (PSG) and the polarization state analyzer (PSA). Each one of these components contains a

J. Innov. Opt. Health Sci. Downloaded from www.worldscientific.com
by UNIVERSITY OF ZARAGOZA on 08/22/23. Re-use and distribution is strictly not permitted, except for Open Access articles.

series of optical elements and devices allowing us to generate and analyze, respectively, any state of polarization. The combined use of PSG and PSA systems allows us to obtain the experimental Mueller matrix images of the samples. The PSG is formed by a linear polarizer oriented at 0° with respect to the laboratory vertical and two parallel aligned liquid crystal (PA-LC) retarders oriented at 45° and 0°, respectively. In the case of the PSA, the elements conforming this arm are the same as in the PSG but located in the inverse order. Since we are collecting images, the PSA includes also a CCD camera to capture the intensity of the sample corresponding to each pixel. As stated, it is straightforward to demonstrate that this architecture for the PSG and PSA allows to generate and measure any possible state of fully polarized light. In addition to that, illumination is provided to the PSG by a light source which can work at three different illumination wavelengths in the visible range (625 nm, 530 nm and 470 nm), thus allowing us to inspect different characteristics of samples. The mobility of both PSG and PSA allows to explore different angular measurement configurations. In this work, we set a particular configuration to measure light scattered by the samples: the sample is illuminated with the PSG located at 34° with respect to the laboratory horizontal and the PSA is at 0° with respect to the laboratory vertical to avoid direct reflections. A visual representation of the setup is shown in Fig. 1.

In the following, we also provide detailed information about the optical components comprising the polarimeter: the illumination is provided by a Thorlabs LED source (LED4D211, operated by DC4104 drivers distributed by Thorlabs) complemented with 10 nm dielectric bandwidth filters distributed by Thorlabs: FB530-10 and FB470-10 for green and blue wavelengths, respectively. The linear polarizer located in the PSG is a Glam–Thompson prism-based CASIX whereas the one placed in the PSA is a dichroic sheet polarizer distributed by Meadowlark Optics. The four PA-LC retarders are variable retarders with temperature control (LVR-200-400-700-1LTSC distributed by Meadowlark Optics). Finally, imaging is performed by means of a 35 mm focal length Edmund Optics TECHSPEC® high resolution objective followed by an Allied Vision manta G-504B CCD camera, with 5 Megapixel GigE Vision and Sony ICX655 CCD sensor, 2452(H) × 2056(V) resolution, and cell size of 3.45 μm × 3.45 μm, so a spatial resolution of 22 μm is achieved.

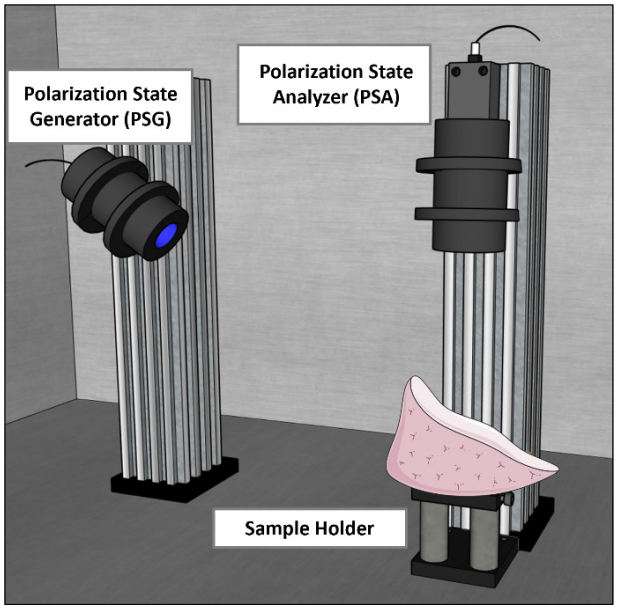

Fig. 1. 3D representation of the complete image Mueller polarimeter composed of the PSG and the PSA. Figure inspired from Ref. 24.

3.2. *Sample preparation*

We want to note that as an internal cross-check designed to ensure the regional accuracy of the depolarization metrics, tissue was submitted to histological analysis. The various samples were provided by a local slaughterhouse and no laboratory animals were used for the experiments; previous treatment and commercial use of the animal tissue was in accordance with Spanish legislation. After acquiring the samples, they were either fresh-prepared for immediate analysis or stored at −16°C before deferred imaging. After polarimetric analysis, regions of interest were cut into blocks of approximately 2.5 × 2.5 cm, formalin-fixed (4%), dehydrated, paraffin-embedded and sliced in 4–6 μm-thick slices, mounted in standard slides, stained with hematoxylin-eosin or Masson technique and analyzed under light microscopy. A detailed protocol of tissue processing and histological techniques is provided in the supplementary files of a previous publication of our group (see Ref. 24).

The pathological description of on of the samples studied in this work is provided in the related sample discussion in the following sections.

J. Innov. Opt. Health Sci. Downloaded from www.worldscientific.com
by UNIVERSITY OF ZARAGOZA on 08/22/23. Re-use and distribution is strictly not permitted, except for Open Access articles.

4. Discriminatory Potential of the IPPs

In this section, we highlight the interest, in terms of discriminatory potential between different depolarizers, of one of the depolarizing triplets reviewed in Sec. 2: the IPPs. Different works have provided that the IPPs are an ideal framework to study depolarizing responses of biological samples,[24–27] being able to increase the image contrast between different structures or even to reveal tissue structures which are hidden when studied through nonpolarimetric images (standard intensity images).

For a better understanding of the IPPs physical interpretation as well as to highlight their potential to discriminate between different depolarizers, in a recent work we provided a series of simple simulations,[34] and the corresponding experimental validation, to study some depolarizers cases in terms of the IPPs, to be compared with the well-known and commonly used depolarization index P_Δ described in Sec. 2.1.[34] The selected depolarizers were constructed as an incoherent addition of very familiar polarizing elements (polarizers, retarders, etc.), which ease the interpretation of the obtained results.

On the one hand, simulated depolarizers were constructed as an incoherent sum of pure matrices of basic polarimetric elements, giving different weights to each Mueller matrix (term) in the addition. On the other hand, experimental validations were implemented by spatially separating the different basic polarimetric elements used in the theoretical addition, and the weights of each element were controlled by properly setting the portion of energy of the input incident light beam illuminating each element. Finally, all those light portions carrying the information of the different polarimetric elements were incoherently integrated in a detector. More details of the simulations and experiments conducted can be consulted in Ref. 34.

By way of illustration, we review the comparison between two depolarizer cases, labeled as depolarizer A and depolarizer B. Regarding the depolarizer A, it was constructed as the incoherent addition of 50% of a linear polarizer oriented at the horizontal direction and 50% of a linear polarizer oriented at the vertical direction. In turn, depolarizer B was constructed as the incoherent addition of 50% of a quarter-waveplate oriented at the horizontal direction, 25% of a half-waveplate oriented at 45° and 25% of the identity matrix (air in the experimental implementation). A sketch of the depolarizers A and B constituent parts is given in Figs. 2(a) and 2(b), respectively. The green spot in the figure represents the illumination beam. The portion of light impinging each material in Figs. 2(a) and 2(b) (specific green area in each material) describes the portion of light that reaches each component of the depolarizers. This light portion (or green area) impinging each element is correlated with the weights for the different light portions, that are incoherently added at the detector.

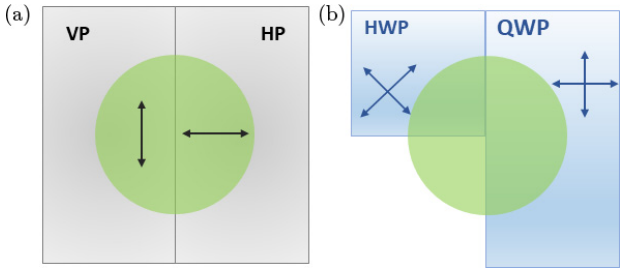

Fig. 2. Optical scheme of the depolarizers (a) A, comprised of a vertical (left) and horizontal (right) polarizer and (b) B, comprised by a half wave plate (HWP) oriented in the horizontal direction, a quarter wave plate (QWP) oriented at 45° and the identity matrix. The green circle indicates the illumination corresponding to each one of the elements conforming the samples.

Table 1. Theoretical and experimental results for the A and B depolarizers.

	Theory				Experiment			
	P_1	P_2	P_3	P_Δ	P_1	P_2	P_3	P_Δ
A	0.00	1.00	1.00	0.57	0.07	0.93	1.00	0.56
B	0.40	0.71	1.00	0.57	0.40	0.70	1.00	0.59

In Table 1, we present the theoretical and experimental results obtained for the two studied depolarizers, in terms of IPPs and P_Δ, which were calculated from corresponding theoretical and experimental Mueller matrices according to the relations provided in Sec. 2.1.

We see how depolarizers A and B are exactly the same sample in terms of P_Δ, but are quite different in terms of IPPs. This result is reinforced by experimental validation. Therefore, even depolarizers A and B are very different structures (see Fig. 2), the global depolarization introduced by such samples is equivalent ($P_\Delta = 0.57$ in both cases), and they are not discriminated by this (commonly used) metric. On the contrary, depolarizers A and B are perfectly discriminated by IPPs, leading to two

J. Innov. Opt. Health Sci. Downloaded from www.worldscientific.com
by UNIVERSITY OF ZARAGOZA on 08/22/23. Re-use and distribution is strictly not permitted, except for Open Access articles.

separated points in the purity space. Therefore, this result points in the direction that in nature, different depolarizing structures, that can be set by different tissues, organization, density, or size of scatter units, etc., even being part of different physical origins, may lead to the same global depolarization, but IPPs arise as interesting tools to discriminate such different structures.

All the aforesaid indicates the usefulness of the IPPs as a discriminative criterion versus the more extended parameter P_Δ. To further highlight the potential of IPPs for biological tissues' visualization, in the following, we provide an illustrative example focusing on different biological structures present in an *ex vivo* animal sample. In particular, we compare the images obtained for the same biological structures for a standard intensity image, for the depolarizing index P_Δ image, and for the three IPPs images. The sample studied corresponds to the endocardial view of a heart section of an *ex vivo* lamb. Obtained images are provided in Fig. 3. We see how depolarizing channels (P_Δ in Fig. 3(e), and P_1, P_2 and P_3 in Figs. 3(b)–3(d), respectively) enhance the visualization of different heart structures, which are invisible or very difficult to observe in the standard intensity image (Fig. 3(a)). For instance, the borders of the different endothelium/endocardium-lined structures such as myocardium proper (Fig. 3), valves, and arterial wall. In addition, in the image corresponding to P_1 channel (Fig. 3(b)), we see the appearance of an almost invisible structure to the rest of the channels which corresponds to the blood capillaries present in the papillary muscles (see yellow arrow). Moreover, in P_1 (Fig. 3(b)) and P_2 (Fig. 3(c)) images, we find a better definition between structures such as the mentioned papillary muscle and the myocardium, that is highly defined in the P_3 image (Fig. 3(d)), and the junction between the muscles and the inner part of the myocardium. Note how in such cases, we achieve finer structure discrimination and definition with P_3 than with the information provided in the P_Δ image (Fig. 3(e)).

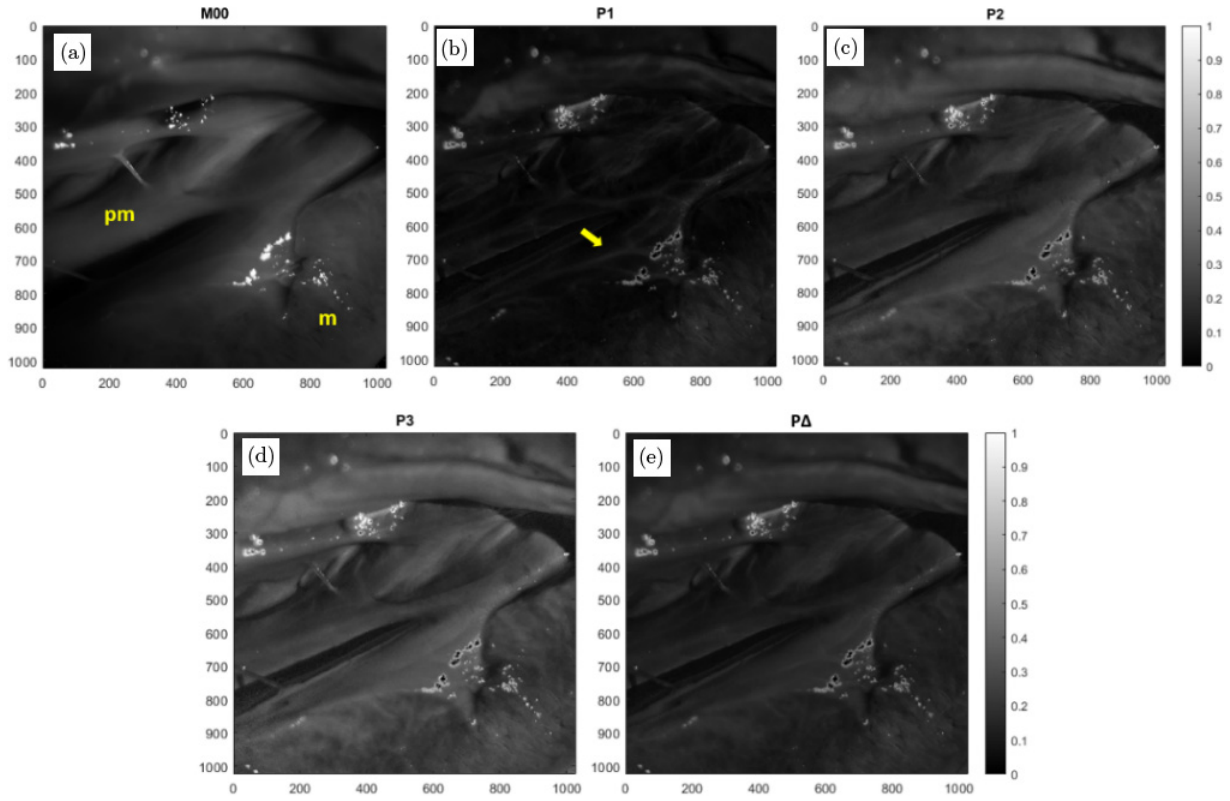

Fig. 3. Polarimetrical analysis of a sample corresponding to an endocardial view of the ventricular cavity with myocardium proper (m) and papillary muscles (pm) (muscular intra-cavitary projections of the myocardium that are essential for valvular stability) including their connective-rich insertion site of the *chordae tendinae* (heart strings), the yellow arrow indicates the blood capillaries present in the pm. (a) is the intensity image, (b), (c) and (d) correspond to the IPPs and (e) is the image corresponding to the depolarization index P_Δ. The value of each polarimetric observable in the figure is coded in a color map where 0 corresponds to black (representing the minimum value of the observables) and 1 to white (representing the maximum values of the observables).

J. Innov. Opt. Health Sci. Downloaded from www.worldscientific.com
by UNIVERSITY OF ZARAGOZA on 08/22/23. Re-use and distribution is strictly not permitted, except for Open Access articles.

As we said before, in this section, we show the raw images of some of the depolarization metrics we find useful for improving contrast and highlighting structures in organic tissue. In particular, we wanted to highlight the usefulness of P_1, P_2 and P_3 for achieving the best results in the analyzed samples. Our aim showing these results is to demonstrate the potential of these observables for organic samples' inspection. In the following sections, we will show different methods where we construct new images allowing us to obtain better results than Fig. 3, but always working with the depolarizing images as a base. With this, we want to encourage researchers working in this field to use these same approaches in their studies or try new ones, always based on images of depolarization observables. In particular, we want to note that there already exist in literature a wide number of image processing methods capable of improving the image contrast of biological structures,[44] and under this scenario, it would be useful to test them directly on polarimetric images, instead of on standard intensity images.

Summarizing, in this section, we provided how the IPPs are very suitable observables to discriminate between different depolarizers, and how this discriminatory potential can be applied for the enhanced visualization of biological tissues, as they are highly depolarizing structures.

5. Biological Tissues Enhanced Vision Through Pseudo-Colored Functions Based on IPPs

In Sec. 4, we provided the potential of the IPPs for enhancing image contrast between different biological structures. As shown in Sec. 2, the IPPs consist of three depolarizing observables (P_1, P_2 and P_3) that can be associated to an orthogonal basis that gives rise to the purity space.[27,33] In this section, we use the IPPs basis to improve the visualization of organic samples through a pseudo-colored approach. In particular, we associate each one of the three IPPs channels corresponding to a given sample with one of the primary colors (red, green and blue) of the RGB color model. The following described results can be further consulted in Refs. 35 and 36.

Given the experimental Mueller matrix of a sample, the corresponding IPPs images can be calculated. Starting from these three images, the first pseudo-colored approach implemented consists of building a linear combination of the IPP images and associating each IPP channel (P_1, P_2 and P_3) to an RGB color. By setting *ad hoc* the weight of each term in the linear combination, we are able to enhance the visualization of certain tissues and structures in biological samples.

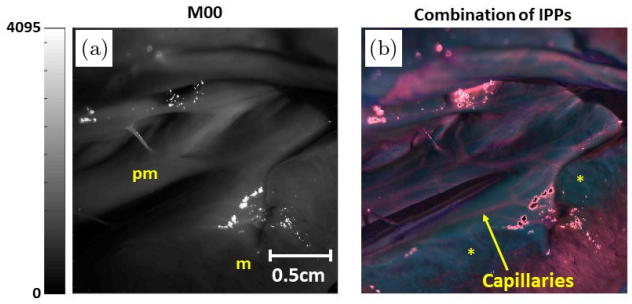

Fig. 4. Polarimetric analysis of an *ex vivo* lamb heart sample, showing an endocardial view of ventricular cavity with solid myocardium (m) and papillary muscle (pm) including their connective rich insertion site ($*$). Where (a) is the intensity image and (b) is the pseudo-colored image obtained by Eq. (16) with $\alpha_1 = 3$, $\alpha_2 = 1$, $\alpha_3 = 1$ where we stand out the capillary structure present in the papillary muscle indicated with the yellow arrow. Image adapted with permission from Ref. 35 © 2017 WILEY-VCH Verlag GmbH & Co. KgaA, Weinheim.

In Fig. 4, we provide an example of the application of this first pseudo-colored approach in biological tissues imaging.[35] For comparison, the analyzed sample is the same endocardial view of an *ex vivo* lamb heart previously discussed in Sec. 4 (see Fig. 3). The particular pseudo-colored image used to visualize the lamb heart is given by

$$C_{\text{pix}}(x,y) = \alpha_1 P_1(x,y) + \alpha_2 P_2(x,y) + \alpha_3 P_3(x,y), \tag{16}$$

where $P_1(x,y)$, $P_2(x,y)$ and $P_3(x,y)$ are the corresponding IPPs images, associated to the red, green and blue colors, and with α_i being the summation weights. The particular weights applied for the lamb heart example are $\alpha_1 = 3$, $\alpha_2 = 1$, $\alpha_3 = 1$, giving larger weight to the P_1 image as it was the one providing larger contrast in certain heart structures, as it is the case of heart blood vessels (see yellow arrow in Fig. 3(b)). Obtained results are shown in Fig. 4, where we compare the standard intensity image of an endocardial view of ventricular cavity (Fig. 4(a)) with the corresponding pseudo-colored image (Fig. 4(b)) implemented according to the above-mentioned. Note how the visualization of the capillaries in the pseudo-colored image is highly enhanced by applying this pseudo-colored approach and could become a very useful tool, for

J. Innov. Opt. Health Sci. Downloaded from www.worldscientific.com
by UNIVERSITY OF ZARAGOZA on 08/22/23. Re-use and distribution is strictly not permitted, except for Open Access articles.

instance, for clinical applications such as surgery, or for the visual recognition of structures. The visualization of other structures as heart valves and cavities and some details of the muscles are also enhanced in the pseudo-colored image.

Note that although visual improvement of biological tissues by using the above-stated pseudo-colored approach is obvious, we note that the choice of the weights was conducted *ad hoc*. Therefore, for each new sample to be studied, a new search for the proper weights must be conducted, which results in a blind search. In this context, to achieve optimized pseudo-colored functions, we also proposed two different approaches and algorithms devised to build automatic pseudo-colored functions.[36] In particular, the two new pseudo-coloration approaches proposed were based on, respectively: (1) the Euclidean distances between mean values of IPPs associated to different tissue classes, and (2) the probability of belonging to a given tissue class according to a Gaussian distribution. Both methods were based on calculating the IPPs mean values for the tissue classes to be discriminated and then, to assign, for each pixel in the final image, a given distance (or probability of belonging, depending on the method) to these tissue classes' mean values. Afterward, each tissue class was assigned to a primary color, and the weight of each color (class) in the final pseudo-colored image was obtained as a function of the above-stated distances-probabilities for each IPPs pixel value. A thorough description of the algorithms applied to construct such optimized pseudo-colored functions can be consulted in Ref. 36.

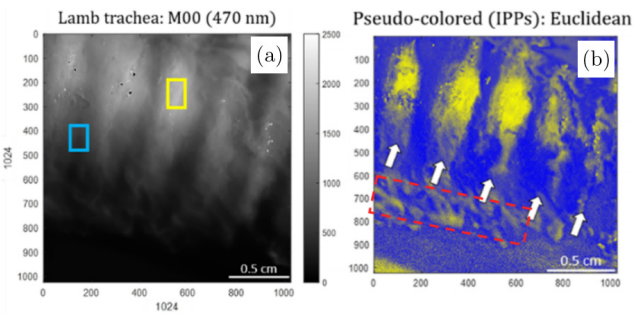

Fig. 5. Intensity (a) and Euclidean pseudo-colored (b) images of a lamb trachea at 470 nm illumination wavelength. Yellow and blue squares show the reference areas corresponding to the trachea ring and sheath, respectively. The arrows in (b) denote the cartilaginous rings and the rectangle is highlighting the trachea border.[36]

As an example, in Fig. 5, we provide the results for a trachea sample corresponding to an *ex vivo* lamb. In particular, in Fig. 5, we compare the image of the trachea section (Fig. 5(a)) with the corresponding pseudo-colored image (Fig. 5(b)). The particular pseudo-colored algorithm used to achieve the image in Fig. 5(b) was based on the Euclidean distances approach, which was the one giving the best results for this particular case. In this sample, two main structures of interest are present, being indicated in Fig. 5(a): the cartilaginous rings (indicated with the yellow square), composed of hyaline cartilage, and the external sheath (indicated with the blue square), also known as tunica adventitia, mainly composed of collagen. These two tissue classes were the ones selected to apply the pseudo-colored functions.

In Fig. 5(b), we see how the cartilaginous rings appear highlighted in yellow and the sheath is colored in blue, increasing the visibility of these two structures. Indeed, the edges of the rings are much more delimited in the pseudo-colored image (Fig. 5(b)) than in the standard intensity image (Fig. 5(a)). Moreover, by applying the pseudo-colored technique, some structures that are invisible in intensity image are visible in the pseudo-colored image. For instance, in Fig. 5(b) the region highlighted with a dashed red rectangle is revealed to correspond to the same kind of tissue as that of the tracheal rings (probably the superposition image of the lateral limbs of each ring).

6. Classification Models Based on Depolarizing Observables

In Sec. 2, we describe different sets of polarimetric observables related to depolarization, including the IPPs. These IPPs are used in Sec. 5 to implement different optical methods for vision enhancement of organic structures. This capability of IPPs, and other depolarizing observables reviewed in Sec. 2, to discriminate between different biological structures can suggest their suitability to be used for automatic classification purposes. In this way, in this section, the depolarizing observables associated to different tissues obtained from a collection of *ex vivo* chicken samples are experimentally measured and used as features for classification purposes.

In particular, in Sec. 6.1, we present the physiological description of the analyzed samples (muscle, tendon, myotendinous junction and bone) extracted

J. Innov. Opt. Health Sci. Downloaded from www.worldscientific.com by UNIVERSITY OF ZARAGOZA on 08/22/23. Re-use and distribution is strictly not permitted, except for Open Access articles.

from the legs of a collection of *ex vivo* chicken samples. In Secs. 6.2 and 6.3, we propose some classification and regression models, respectively, useful for the automatic classification of the stated tissues. Importantly, all the implemented classification models are based on the depolarization metrics above stated.

6.1. *Sample description*

The structural properties of different tissues are directly related to the different values of the polarimetric observables, depending on their histologic structure and functionality. Therefore, here we provide a brief physiological analysis of the different chicken structures studied. The chicken tissues analyzed in this work are skeletal muscle, tendon, myotendinous junction and bone. The skeletal muscle is composed of bundles of long, fusiform, multinucleated cells filled with contractile myofibrils and organized into fascicles surrounded both individually (perimysium) and collectively (epimysium) by sheets of collagen-rich tissue.[45] Tendons are composed of parallel fascicles of collagen following the same directionality as the corresponding muscle.[46] A collagenous fascia covers both muscle and tendon.[47] Myotendinous junction is a variable combination of both previously described tissues. They are progressively intermixed following a continuum along the muscle-tendon transition. Finally, bones are composed of a dense matrix of collagen fibers arranged following both the axis of the bone and concentrically surrounding every *lacuna* (spaces containing cells that are dispersed through the bone). Mineral deposits are in the collagen fibers and, particularly, in the spaces between adjacent collagen fibers.

6.2. *Organic tissues classification models based on depolarizing observables*

Different works have reported an interest in using classification algorithms for biological tissues recognition.[23,24,27] By taking into account the potential of depolarizing observables to discriminate between organic tissues discussed in the previous sections, we have studied the interest of implementing different classification models previously trained with depolarizing data. For the model construction, we selected three well-known supervised machine learning classifiers included in the "Statistics and Machine Learning Toolbox" of the MATLAB software: the decisiontree classifier, the linear discriminant analysis for classification and the k-nearest neighbor (kNN) classifier.[48–50] These three algorithms were trained by using data corresponding to different depolarization metrics triplets (those corresponding to the depolarizing spaces described in Sec. 2 and reported in Ref. 33), obtained from the experimental Mueller matrices measured at three different wavelengths (625 nm, 530 nm and 470 nm) of a collection of *ex vivo* chicken samples. In particular, three different types of chicken tissues were inspected: tendon, muscle and myotendinous junction tissues (described in Sec. 6.1).

From all the trained models, we observe that the kNN classifier had the best performance with the best accuracy in terms of tissue classification. For this reason, the subsequent discussion is focused on comparing the performance of kNN models trained with different depolarizing triplets, but results corresponding to other classifiers (based on other algorithms) can be consulted in Ref. 27. In particular, the performance of five different kNN classification models trained with a different set of features ((1) natural space data, (2) IPPs data, (3) high-order depolarization index data, (4) the canonical space metrics data and (5) the type I Lorentz parameters data) is presented in Table 2 in terms of percentage of well-classified tissues. In addition, this is provided for tissues illuminated with three different wavelengths (625 nm, 530 nm and 470 nm; different rows in Table 2). As can be observed in Table 2, the best classification performance (65% of well-classified tissues for an illumination wavelength of 625 nm) is obtained when training the models with natural space data as well as with IPPs data, i.e., with those metrics based on the H eigenvalues (see Sec. 2). This can be understood if taking into account that these two depolarizing spaces lead to the larger volumes within the studied spaces, and this situation can be interpreted as larger discriminatory capacity.[27] In addition, if analyzing the models performance as a function of the used wavelength, we realize that the best results are obtained for red illumination (625 nm). This can be connected with the fact that larger wavelengths penetrate deeper in soft tissues, and therefore, more physical information can be encoded in depolarization content through light-matter interactions.[51] Interestingly, the above-reported study was

Table 2. Percentage of well-classified tissues as a function of the wavelength and the depolarization parameter for the kNN classification method.

	Eigenvalue-based depolarization metrics			Canonical-based depolarization metrics	
Wavelength (nm)	$\lambda_1, \lambda_2, \lambda_3$	P_1, P_2, P_3	$P_\Delta, P_\Delta^{(3)}, P_\Delta^{(4)}$	d_1, d_2, d_3	$L_I, L_I^{(3)}, L_I^{(4)}$
625	65	65	60	60	55
530	59	59	50	64	50
470	60	59	52	62	49

improved in Ref. 52 by training the classification algorithms simultaneously with data coming from multiple wavelengths (625 nm, 530 nm and 470 nm), i.e., increasing the number of features used for training our kNN models, achieving global accuracies of 86%.

6.3. *Organic tissues classification and visualization based on a regression model on depolarizing data*

In this section, we used regression models combined with polarimetric data for classification.[24] This approach is different than the one discussed in Sec. 6.2, with models based on different classification algorithms.

In particular, we started the study by measuring the Mueller matrix of the four tissues classes described in Sec. 6.1 (bone, muscle, tendon and myotendinous junction) from a statistical representative collection of *ex vivo* chicken samples. This was conducted for three different wavelengths (625 nm, 530 nm and 470 nm). From each Mueller matrix measured, for each of the four tissues classes, we calculated a series of representative polarimetric observables, that focuses in the main polarimetric responses of samples (retardance, dichroism and depolarization). In particular, the observables selected were: the Polarizance (P), representing the capability of a sample to polarize a fully depolarized light, the Diattenuation (D), representing the dependence of the exiting intensity with the incident state of polarization, the total Retardance (R), stating the phase difference introduced by the sample, the linear retardance (δ), providing the retardance corresponding to the associated linear retarder and the optical rotation (ψ), giving the orientation of neutral axes of the associated linear retarder. Further description of these metrics and their physical interpretation can be consulted in Refs. 32 and 52. In addition to the above-stated polarimetric observables, we also included depolarizing measures as input data. In particular, from the depolarizing spaces described in Sec. 2, we included the IPPs into the study, as they provided their suitability to the analysis of biological samples (see Secs. 4 and 5). Finally, the depolarization index P_Δ (see Sec. 2) was also included in the study because it is a widely used metric in biomedical applications.

After analyzing the data behavior corresponding to the obtained measures, we realized that they do not follow a normal distribution, so nonparametric statistics were required. Consequently, we applied a logistic regression on polarimetric data, as it is valid for nonparametric distributions. However, before applying the regression, we conducted a principal component analysis (PCA), achieving the principal components as a function of the polarimetric parameters.[53,54] Specifically, the logistic regression was applied to obtained principal components, because in this way, we ensure a convergent solution. In addition, transforming the polarimetric space to the principal component space allowed us to reduce the initial 27 variables (nine observables for three wavelengths) to a set of independent predictor variables which maintain the information contained in the original metrics describing an adequate proportion of the variance of the initial data.[24] In particular, our PCA analysis reduced the number of variables creating a 10-dimension space explaining more than 90% of the original metrics variance.

Before applying the logistic regression on principal components data space, we analyzed the discrimination potential of these particular factors. To do so, the receiver operating characteristic (ROC) curve analysis was used as a criterion to describe the discriminatory potential of each principal component.[55,56] Usually, to compare the performance of different classifiers it is common to calculate their corresponding area under the curve (AUC). The

J. Innov. Opt. Health Sci. Downloaded from www.worldscientific.com by UNIVERSITY OF ZARAGOZA on 08/22/23. Re-use and distribution is strictly not permitted, except for Open Access articles.

J. Innov. Opt. Health Sci. Downloaded from www.worldscientific.com by UNIVERSITY OF ZARAGOZA on 08/22/23. Re-use and distribution is strictly not permitted, except for Open Access articles.

Table 3. AUC for the 10 principal components for the different tissues.

	Muscle	Tendon	Myotendinous junction	Bone
C_1	**0.733**	0.699	**0.754**	**0.734**
C_2	0.559	0.717	0.567	0.577
C_3	0.528	0.651	0.583	0.512
C_4	0.731	**0.745**	0.563	0.542
C_5	0.667	0.733	0.500	0.527
C_6	0.516	0.714	0.521	0.725
C_7	0.567	0.567	0.508	0.722
C_8	0.703	0.706	0.544	0.649
C_9	0.581	0.540	0.616	0.507
C_{10}	0.569	0.495	0.623	0.601

AUC values are restricted from 0, corresponding to no predictive capability to 1, where sensitivity and specificity are 100%. The AUC values for each of the 10 principal components are provided in Table 3.

As a convention, it is generally assumed that values of AUC larger than 0.5 present a certain discrimination potential. In our case, the larger AUC values when studying the principal components are found for C_1 and C_4 components (highlighted in bold in Table 3). In particular, the C_1 parameter presents the larger discriminatory potential for the muscle, the myotendinous junction and the bone tissues, whereas the C_4 channel gives the best result for the tendon.

The last step was to apply the logistic function to fit polarimetric data through the principal components space. The logistic function is written as follows:

$$p = \frac{1}{1 + e^{-(\beta_0 + \sum_i^n \beta_i C_i)}}, \tag{17}$$

where C_i are the i principal components, β_i the weights of each component and β_0 a constant value. Equation (17) is restricted between 0 and 1, its values interpreted as the probability of a given outcome. As we are dealing with four different tissues, four different logistic regressions were conducted on the data (each one for their corresponding tissue data class). This situation led us to four models each one capable of giving the probability of a certain tissue belonging to a specific tissue class. The explicit function of the four achieved models can be consulted in Ref. 24. To quantify the accuracy of the obtained models, in Table 4, we present their corresponding specificity and sensitivity values (two parameters usually employed in the medical field to evaluate the accuracy of a predictive model).

Table 4. Sensitivity and Specificity values of each predictive model.

	Muscle	Tendon	Myotendinous junction	Bone
Sensitivity (%)	86.0	85.3	82.0	82.6
Specificity (%)	88.8	93.5	71.0	80.6

By considering the results in Table 4, we obtain high sensitivity and specificity values for the predictive model for muscle, tendon and bone, obtaining values higher than 80% in all cases. In this sense, the results obtained for tendon are especially noticeable with a sensitivity of 83.5% and a specificity of 93.5%. The worst obtained results correspond to the myotendinous junction tissue, with a specificity of 71%. However, this agrees with the physiological description of the tissues (Sec. 6.1), being the myotendinous tissue a transition between muscle and tendon. This physical nature of the myotendinous junction makes it more difficult to discriminate between muscle and tendon, as they present very high morphological and physiological similarities.

Once we built the four probabilistic functions above-stated, we applied them for imaging recognition. In particular, for a given unknown tissue image, the four models can be applied pixel-to-pixel, assigning in each case a certain probability belonging to a certain tissue class.

As an example, in the following, we show this particular situation applied to the study of a tendon. An arbitrary tendon image, not belonging to the database used to train the models, was tested. In particular, from the Mueller matrix of an arbitrary chicken tendon, we extracted all the polarimetric observables above-described and they were transformed to the principal components space. With the β_i coefficients corresponding to the already constructed models, and using the principal components related to the new tendon, the function shown in Eq. (17) was implemented for each tissue class. This was conducted pixel-to-pixel, so four images were obtained, each one providing the probability of each pixel to belong to a certain tissue class. Results are shown in Fig. 6, where the different probability images are represented in gray scale (the black assigned for 0 probability and the white for probability equal to 1). The corresponding intensity image for the studied tendon is given in Fig. 6(a). Figure 6(b) provides the probability image when applying the muscle model to analyze

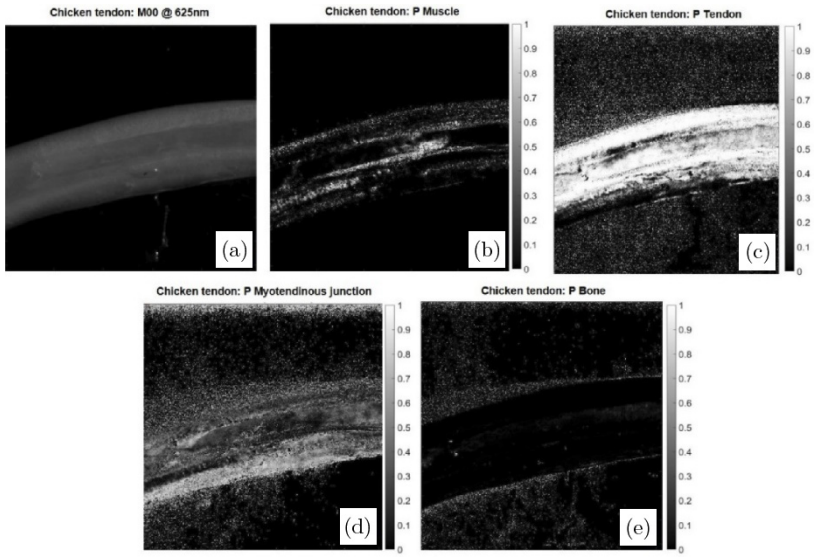

Fig. 6. (a) Intensity image and images of the probability of the different tissue classification when applying: (b) the muscle-model, (c) tendon-model, (d) myotendinous junction-model and (e) bone-model on a tendon sample. The gray level bars indicate the probability of each pixel to be recognized as a particular tissue. Image [adapted] with permission from Ref. 24 © The Optical Society.

the tendon; Fig. 6(c) provides the probability image when applying the tendon model to analyze the tendon; Fig. 6(d) provides the probability image when applying the myotendinous junction probabilistic model to analyze the tendon; and finally, Fig. 6(e) provides the probability image when applying the bone model to analyze the tendon. The ideal result would be the tendon completely painted in white for Fig. 6(c), and the tendon completely painted in black for the other cases. Considering results given in Fig. 6, we see that, indeed, the tendon regression model satisfactorily recognizes the tendon as a tendon, and we see that the other regression models do not recognize the tendon as muscle, myotendinous junction or bone, this providing the suitability of regression models to be applied for automatic classification of tissue images. In the case of the myotendinous junction, the probability image (Fig. 6(d)) shows a higher number of points closer to white than the other tissue classes (bone and muscle). As stated before, this is in concordance with the physiological characteristic of the myotendinous junction described in Sec. 6.1, having very similar properties to muscle and tendon tissues.

Summarizing, in this section, we have presented two different approaches for organic tissue classification, using both classification and regression models trained with different polarimetric observables. We retrieve excellent results when applying the proposed models to the inspected biological sample. Importantly, although these studies were performed on chicken samples, the methods can be extrapolated to different animal or human tissues, with potential within biomedical applications.

7. Conclusions

We have presented some results related to the use of depolarization metrics in the biomedical applications field. We have found that the depolarization observables are very adequate tools for the analysis and visualization of biological tissues. Interestingly, we highlighted the usefulness of a particular depolarizing observables triplet, the so-called IPPs, as the most promising candidates for these applications.

First, to ease the understanding of IPPs metrics, we provided a set of simulations and experiments, based on synthesized depolarizers constructed by the incoherent addition of basic polarimetric elements, of a very easy physical interpretation, and that highlighted the use of IPPs as ideal depolarizing space for discriminate between different depolarizers.

As tissues behave as depolarizers by scattering light (among other physical mechanisms), we applied this discriminatory capability of IPPs to show how IPPs images highly improve the contrast between different organic tissues, and they are even able to reveal structures hidden in standard intensity images. Furthermore, we also show how they lead to enhanced vision of biological tissues

J. Innov. Opt. Health Sci. Downloaded from www.worldscientific.com
by UNIVERSITY OF ZARAGOZA on 08/22/23. Re-use and distribution is strictly not permitted, except for Open Access articles.

J. Innov. Opt. Health Sci. Downloaded from www.worldscientific.com
by UNIVERSITY OF ZARAGOZA on 08/22/23. Re-use and distribution is strictly not permitted, except for Open Access articles.

when compared with the depolarization index P_Δ, a well-known and commonly used parameter for studying depolarization effects in biological tissues. Furthermore, to take advantage of this visualization enhancement by means of the IPPs, we build different pseudo-colored methods resulting in better visualization enhancement of organic tissue structures. The proposed methods for biological tissues visualization arise as potential tools for clinical applications for pathology detection or guided surgery.

Finally, once we demonstrated the potential of these depolarization metrics in the biomedical framework, we studied their suitability for classification purposes. Under this scenario, different classification methods are presented in this work. The implemented models are based on classification and regression algorithms trained with polarimetric data obtained from the experimental Mueller matrices measured on four different tissues (bone, muscle, tendon and myotendinous junction) of statistically significant collection of *ex vivo* chicken samples. Note that although in this case, the methods are applied for animal tissues (achieving very satisfying results in terms of predictive performance) they can be adapted from animal to human samples. We want to note that the classification methods presented in this work, applied on *ex vivo* animal tissues, pave the way for future studies in human tissues. In this sense, although the efficiency of the provided metrics has not been tested for human applications, as for instance, to test their suitability for the early detection of certain pathologies, the excellent classification results obtained for animal tissue classification seem to indicate that such metrics are ideal to be tested in biomedical applications. In this sense, some first results are being published in specialized literature.[57]

Acknowledgments

We acknowledge the financial support of Spanish MINECO (PID2021-126509OB-C21, and Fondos FEDER); Catalan Government (2017-SGR-001500).

Conflicts of Interest

The authors declare that there are no conflicts of interest relevant to this article.

References

1. T. Fan, G. Xu, J. Teng, Y. Li, X. Zhang, C. Wang, P. Xu, Y. Yan, X. Xu, "Polarimetry-inspired feature fusion spectroscopy (PIFFS) for ammonia sensing in water," *Opt. Express* **30**, 18415–18433 (2022).
2. M. Asgarimehr, M. Hoseini, M. Semmling, M. Ramatschi, A. Camps, H. Nahavandchi, R. Haas, J. Wickert, "Remote sensing of precipitation using reflected gnss signals: Response analysis of polarimetric observations," *IEEE Trans. Geosci. Remote Sens.* **60**, 1–12 (2022).
3. M. Honda, R. Tazaki, K. Murakawa, H. Terada, T. Kudo, T. Hattori, J. Hashimoto, M. Tamura, M. Watanabe, "Subaru/IRCSL-band spectropolarimetry of the hd142527 disk scattered light," *Publ. Astron. Soc. Jpn.* **74**, 851–856 (2022).
4. A. van Eeckhout, E. Garcia-Caurel, T. Garnatje, J. C. Escalera, M. Durfort, J. Vidal, J. J. Gil, J. Campos, A. Lizana, "Polarimetric imaging microscopy for advanced inspection of vegetal tissues," *Sci. Rep.* **11**(1), 3913 (2021).
5. C. H. Lucas Patty, D. A. Luo, F. Snik, F. Ariese, W. J. Buma, I. L. ten Kate, R. J. M. van Spanning, W. B. Sparks, T. A. Germer, G. Garab, M. W. Kudenov, "Imaging linear and circular polarization features in leaves with complete Mueller matrix polarimetry," *Bioc. et Bio. Acta (BBA) — General Subjects* **1862**(6), 13501363 (2018).
6. N. Ghosh, I. A. Vitkin, "Tissue polarimetry: Concepts, challenges, applications, and outlook," *J. Biomed. Opt.* **16**(11), 110801 (2011).
7. L. V. Wang, G. L. Coté, S. L. Jacques, "Special section guest editorial: Tissue polarimetry," *J. Biomed. Opt.* **7**, 278 (2002).
8. A. G. Clark, D. M. Vignjevic, "Modes of cancer cell invasion and the role of the microenvironment," *Curr. Opt. Cell Biol.* **36**, 13–22 (2015).
9. M. Kupinski, M. Boffety, F. Goudail, R. Ossikovski, A. Pierangelo, J. Rehbinder, J. Vizet, T. Novikova, "Polarimetric measurement utility for pre-cancer detection from uterine cervix specimens," *Biomed. Opt. Express* **9**, 5691–5702 (2018).
10. J. Chue-Sang, N. Holness, M. Gonzalez, J. Greaves, I. Saytashev, S. Stoff, A. Gandjbakhche, V. Chernomordik, G. Burkett, J. Ramella-Roman, "Use of Mueller matrix colposcopy in the characterization of cervical collagen anisotropy," *J. Biomed. Opt.* **23**(12), 1–9 (2018).
11. J. Sprenger, C. Murray, J. Lad, B. Jones, G. Thomas, S. Nofech-Mozes, M. Khorasani, A. Vitkin, "Toward a quantitative method for estimating tumour-stroma ratio in breast cancer using polarized light microscopy," *Biomed. Opt. Express* **12**, 3241–3252 (2021).

J. Innov. Opt. Health Sci. Downloaded from www.worldscientific.com
by UNIVERSITY OF ZARAGOZA on 08/22/23. Re-use and distribution is strictly not permitted, except for Open Access articles.

12. V. A. Ushenko, B. T. Hogan, A. Dubolazov, G. Piavchenko, S. L. Kuznetsov, A. G. Ushenko, Y. O. Ushenko, M. Gorsky, A. Bykov, I. Meglinski, "3D Mueller matrix mapping of layered distributions of depolarization degree for analysis of prostate adenoma and carcinoma diffuse tissues," *Sci. Rep.* **11**(1), 5162 (2021).
13. V. A. Ushenko, B. T. Hogan, A. Dubolazov, A. V. Grechina, T. V. Boronikhina, M. Gorsky, A. G. Ushenko, Y. O. Ushenko, A. Bykov, I. Meglinski, "Embossed topographic depolarization maps of biological tissues with different morphological structures," *Sci. Rep.* **11**(1), 3871 (2021).
14. E. Du, H. He, N. Zeng, M. Sun, Y. Guo, J. Wu, S. Liu, H. Ma, "Mueller matrix polarimetry for differentiating characteristic features of cancerous tissues," *J. Biomed. Opt.* **19**(7), 076013 (2014).
15. J. S. Baba, J. Chung, A. H. DeLaughter, B. D. Cameron, G. L. Cote, "Development and calibration of an automated Mueller matrix polarization imaging system," *J. Biomed. Opt.* **7**(3), 341–349 (2002).
16. P. Schucht, H. R. Lee, H. M. Mezouar, E. Hewer, A. Raabe, M. Murek, I. Zubak, J. Goldberg, E. Kövari, A. Pierangelo, T. Novikova, "Visualization of white matter fiber tracts of brain tissue sections with wide-field imaging Mueller polarimetry," *IEEE Trans. Med. Imaging* **39**(12), 4376–4382 (2020).
17. O. Rodríguez-Núñez, P. Schucht, E. Hewer, T. Novikova, A. Pierangelo, "Polarimetric visualization of healthy brain fiber tracts under adverse conditions: *ex vivo* studies," *Biomed. Opt. Express* **12**, 6674–6685 (2021).
18. Z. Ali, T. Mahmood, A. Shahzad, M. Iqbal, I. Ahmad, "Assessment of tissue pathology using optical polarimetry," *Lasers Med. Sci.* **37**, 1907–1919 (2022).
19. C. He, H. He, J. Chang, B. Cheng, H. Ma, M. J. Booth, "Polarisation optics for biomedical and clinical applications: A review," *Light Sci. Appl.* **10**, 194 (2021).
20. J. Qi, D. S. Elson, "Mueller polarimetric imaging for surgical and diagnostic applications: A review," *J. Biophoton.* **10**(8), 950–982 (2017).
21. H. He, R. Liao, N. Zeng, P. Li, Z. Chen, X. Liu, H. Ma, "Mueller matrix polarimetry — an emerging new tool for characterizing the microstructural feature of complex biological specimen," *J. Light. Technol.* **37**(11), 2534–2548 (2019).
22. J. C. Ramella-Roman, I. Saytashev, M. Piccini, "A review of polarization-based imaging technologies for clinical and preclinical applications," *J. Opt.* **22**, 123001 (2020).
23. C. Heinrich, J. Rehbinder, A. Nazac, B. Teig, A. Pierangelo, J. Zallat, "Mueller polarimetric imaging of biological tissues: classification in a decision-theoretic framework," *J. Opt. Soc. Am. A* **35**, 2046–2057 (2018).
24. C. Rodriguez, A. van Eeckhout, L. Ferrer, E. Garcia-Caurel, E. González-Arnay, J. Campos, A. Lizana, "Polarimetric data-based model for tissue recognition," *Biomed. Opt. Express* **12**(8), 4852–4872 (2021).
25. D. Ivanov, V. Dremin, E. Borisova, A. Bykov, T. Novikova, I. Meglinski, R. Ossikovski, "Polarization and depolarization metrics as optical markers in support to histopathology of *ex vivo* colon tissue," *Biomed. Opt. Express* **12**, 4560–4572 (2021).
26. R. Meng, H. He, T. Liu, T. Sun, H. Ma, "Quantitative detection and comparison of liver tissues using label-free Mueller matrix microscope," *Proc. SPIE 10877*, Dynamics and Fluctuations in Biomedical Photonics XVI **10877**, 101–108 (2019).
27. A. van Eeckhout, E. Garcia-Caurel, R. Ossikovski, A. Lizana, C. Rodríguez, E. González-Arnay, J. Campos, "Depolarization metric spaces for biological tissues classification," *J. Biophoton.* **13**, e202000083 (2020).
28. S. L. Jacques, J. C. Ramella-Roman, K. Lee, "Imaging skin pathology with polarized light," *J. Biomed. Opt.* **7**(3), 329–340 (2002).
29. S. Manhas, M. K. Swami, H. S. Patel, A. Uppal, N. Ghosh, P. K. Gupta, "Polarized diffuse reflectance measurements on cancerous and noncancerous tissues," *J. Biophoton.* **2**, 581–587 (2009).
30. J. Chung, W. Jung, M. J. Hammer-Wilson, P. Wilder-Smith, Z. Chen, "Use of polar decomposition for the diagnosis of oral precancer," *Appl. Opt.* **46**, 3038–3045 (2007).
31. A. Pierangelo, A. Benali, M.-R. Antonelli, T. Novikova, P. Validire, B. Gayet, A. De Martino, "*Ex vivo* characterization of human colon cancer by Mueller polarimetric imaging," *Opt. Express* **19**, 1582–1593 (2011).
32. J. J. Gil, R. Ossikovski, *Polarized Light and the Mueller Matrix Approach*, CRC Press, Boca Raton (2016).
33. R. Ossikovski, J. Vizet, "Eigenvalue-based depolarization metric spaces for Mueller matrices," *J. Opt. Soc. Am. A* **36**, 1173–1186 (2019).
34. A. van Eeckhout, A. Lizana, E. Garcia-Caurel, J. J. Gil, R. Ossikovski, J. Campos, "Synthesis and characterization of depolarizing samples based on the indices of polarimetric purity," *Opt. Lett.* **42** (20), 4155–4158 (2017).
35. A. van Eeckhout, A. Lizana, E. Garcia-Caurel, J. J. Gil, A. Sansa, C. Rodríguez, I. Estévez, E. González, J. C. Escalera, I. Moreno, J. Campos, "Polarimetric imaging of biological tissues based on the indices of polarimetric purity," *J. Biophoton.* **11**, e201700189 (2017).

J. Innov. Opt. Health Sci. Downloaded from www.worldscientific.com
by UNIVERSITY OF ZARAGOZA on 08/22/23. Re-use and distribution is strictly not permitted, except for Open Access articles.

36. C. Rodriguez, A. van Eeckhout, L. Ferrer, E. Garcia-Caurel, A. Lizana, J. Campos, "Authomatic pseudo-coloring approaches to improve visual perception and contrast in polarimetric images of biological tissues," *Sci. Rep.* **12**(1), 18479 (2022).
37. S. R. Cloude, "Conditions for the physical realizability of matrix operators in polarimetry," *Proc. SPIE* **1166**, 177–185 (1989).
38. S. R. Cloude, "Group theory and polarization algebra," *Optik* **75**, 26–36 (1986).
39. I. San José, J. J. Gil, "Invariant indices of polarimetric purity. Generalized indices of purity for $n \times n$ covariance matrices," *Opt. Commun.* **284**, 38–47 (2011).
40. J. J. Gil, E. Bernabeu, "Depolarization and polarization indices of an optical system," *Opt. Acta* **33**(2), 185–189 (1986).
41. J. J. Gil, "Review on Mueller matrix algebra for the analysis of polarimetric measurements," *J. Appl. Remote Sens.* **8**(1), 081599 (2014).
42. R. Ossikovski, "Canonical forms of depolarizing Mueller matrices," *J. Opt. Soc. Am. A* **27**, 123–130 (2010).
43. R. Ossikovski, "Analysis of depolarizing Mueller matrices through a symmetric decomposition," *J. Opt. Soc. Am. A* **26**, 1109–1118 (2009).
44. S. Uchida, "Image processing and recognition for biological images," *Biomed. Develop. Growth Differ.* **55**, 523–549 (2013).
45. B. Charvet, F. Ruggiero, D. Le Guellec, "The development of the myotendinous junction: A review," *Musc. Liga. Tend. J.* **2**(2), 53–63 (2012).
46. R. James, G. Kesturu, G. Balian, A. B. Chhabra, "Tendon: biology, biomechanics, repair, growth factors, and evolving treatment options," *J. Hand Surg. Am.* **33**(1), 102–112 (2008).
47. S. Schiaffino, C. Reggiani, "Fiber types in mammalian skeletal muscles," *Physiol. Rev.* **91**(4), 1447–1531 (2011).
48. L. Breiman, J. H. Friedman, R. A. Olshen, C. J. Stone, *Classification and Regression Trees*, Chapman & Hall, Boca Raton (1984).
49. Y. Guo, T. Hastie, R. Tibshirani, "Regularized linear discriminant analysis and its application in microarrays," *Biostatistics* **8**(1), 86 (2007).
50. T. Mitchell, *Machine Learning*, McGraw-Hill, NewYork (1997).
51. F. H. Mustafa, M. S. Jaafar, "Comparison of wavelength-dependent penetration depths of lasers in different types of skin in photodynamic therapy," *Indian J. Phys.* **87**(3), 203–209 (2013).
52. A. van Eeckhout, E. Garcia-Caurel, R. Ossikovski, A. Lizana, C. Rodríguez, E. González-Arnay, J. Campos, "Depolarizing spaces for biological tissue classification based on a wavelength combination," *Proc. SPIE 11363, Tissue Optics and Photonics* (2020), p. 113631G.
53. H. H. Jolliff, "Principal component factor analysis," *All Grad. Plan B Rep.* 1117 (1968).
54. V. Srinivasarao, U. Ghanekar, "Speech enhancement — an enhanced principal component analysis (EPCA) filter approach," *Comput. Electr. Eng.* **85**, 106657 (2020).
55. T. Fawcett, "An introduction to ROC analysis," *Pattern Recognit. Lett.* **27**(8), 861–874 (2006).
56. J. A. Cook, "ROC curves and nonrandom data," *Pattern Recognit. Lett.* **85**, 35–41 (2017).
57. D. Ivanov, V. Dremin, T. Genova, A. Bykov, T. Novikova, R. Ossikovsky, I. Meglinski, "Polarization-based histopathology classification of *ex vivo* colon samples supported by machine learning," *Front. Phys.* **9**, 814787 (2022).